MAX-PLANCK-INSTITUT FÜR PLASMAPHYSIK

GARCHING BEI MÜNCHEN

Soft X-Ray Diagnostics for ASDEX Upgrade

M. Bessenrodt-Weberpals, J. C. Fuchs, M. Sokoll,
and the ASDEX Upgrade Team

IPP 1/290 August 1995

Die nachstehende Arbeit wurde im Rahmen des Vertrages zwischen dem Max-Planck-Institut für Plasmaphysik und der Europäischen Atomgemeinschaft über die Zusammenarbeit auf dem Gebiete der Plasmaphysik durchgeführt.

Abstract

This paper presents the soft X-ray pinhole camera system for the ASDEX Upgrade medium-size tokamak. Details of the optical system and the detectors in use are given. Special emphasis is put on the specific data acquisition with high-performance parallel computing. Data analysis is performed by rotational tomographic reconstruction in natural coordinates and by different transformation techniques (FFT, wavelet, singular value decomposition). First results with the system are presented for recent H-mode discharges. They are characterized by frequent and weak type-III ELMs in the outer plasma zones and a rotating helical (1,1) MHD structure in the core plasma.

PACS numbers : 0785, 5225, 5230, 5255, 5270.

Contents

1 Introduction

Hot fusion plasmas with temperatures of a few keV have their maximum radiation in the soft X-ray (SXR) spectral region.[1] The detection of SXR radiation from a fusion plasma is thus a well-suited diagnostics for various purposes, namely for impurity investigations as well as for the study of MHD activities.

The corresponding energy spectrum consists of a continuum of free-free bremsstrahlung, free-bound recombination radiation, and bound-bound line radiation (with minor contributions). For a Maxwellian plasma and hydrogenic bremsstrahlung, the radiated power $d\epsilon$ per unit volume in the photon energy interval dE reads

$$\left(\frac{d\epsilon}{dE}\right)_{ff} = \alpha\, n_e^2\, Z_{\text{eff}}\, g_{ff}(T_e, E) \frac{\exp(-E/T_e)}{\sqrt{T_e}}.$$

It depends strongly on the electron temperature T_e [keV], the electron density n_e [10^{13} cm^{-3}], and the impurity content, which determines the effective charge $Z_{\text{eff}} = \sum_i n_i Z_i^2 / n_e$; $\alpha = 3 \times 10^{11}$ is a constant, and $g_{ff}(T_e, E)$ denotes the temperature-averaged gaunt factor. Especially, it is $(d\epsilon/dE)_{ff}^{(Z)} / (d\epsilon/dE)_{ff}^{(H)} = Z_{\text{eff}}$. Usually, the quantity γ denotes the contribution of bremsstrahlung to the measured total radiation, i.e. $(d\epsilon/dE)_{tot} = \gamma\ (d\epsilon/dE)_{ff}$, and ζ describes the enhancement of the measured total radiation in relation to the hydrogenic bremsstrahlung $(d\epsilon/dE)_{ff}^{(H)}$ due to impurity effects, i.e. $(d\epsilon/dE)_{tot} = \zeta\ (d\epsilon/dE)_{ff}^{(H)}$. Thus, it is $\zeta = \gamma\, Z_{\text{eff}}$.

This paper presents the SXR pinhole camera system for the ASDEX Upgrade medium-size tokamak ($R_0 = 1.65$ m, $a = 0.5$ m, $\kappa = 1.6$, $I_p \leq 1.4$ MA, $B_t \leq 3.9$ T, $P_{\text{aux}} \leq 15$ MW). Section 2 gives details of the optical system and the detectors in use and Section 3 deals with the specific data acquisition with high-performance parallel computing. Section 4 is devoted to the tomographic reconstruction methods which have been applied to analyse the SXR signals, which are integrals along the lines of sight. Transformation techniques like FFT, wavelet, singular value decomposition are considered in Section 5. First results with the system are given in Section 6. Finally, a summary is given and some conclusions are drawn in Section 7.

[1] SXR radiation is defined as radiation with energies between 100 eV and 10 keV as compared with X-ray radiation between 1 keV to 100 keV on the high-energy side and with vacuum ultraviolet radiation between 6 eV and 1 keV on the low-energy side. With respect to wavelength, 1 keV corresponds to 1.24 nm.

2 Camera system

For the SXR radiation under discussion, it is convenient to use pinhole cameras with semiconductor detectors. Details of the ASDEX Upgrade camera system are given below.

2.1 Detectors

The detectors inside the pinhole cameras are passivated ion-implanted silicon diodes (manufactured by Intertechnique). These are made of pure silicon with a thickness $d_3 = 300$ μm and an active layer of width $d_1 = 2.6$ mm and length $d_2 = 8.6$ mm. On the front side of the diode, where the photons enter, there is a coating with 200 nm aluminum. As a consequence, a p-n transition is built up between the aluminum layer and silicon substrate. On the rear side, the diode is coated with 150 nm aluminum in order to electrically contact the diode.

Photons which enter the detector produce electron-hole pairs by the photoelectric effect; one pair needs 3.62 eV of absorbed energy. Hence, the absolute sensitivity of the diode reaches $\gamma_D = 1\text{A}/3.62\text{W} = 0.276$ A/W. If the electric field in the diode exceeds a critical threshold, all electron-hole pairs may be separated with a probability equal to 1. Normally, the diode is operated with negative voltage, i.e. in reverse bias mode. This builds up an electric field which is directed from the rear to the front side and thereby rectifies the current. The ASDEX Upgrade system is usually operated with -25 V bias voltage; generally, the diode X-ray response is insensitive to large changes in the detector bias voltage [WENZEL and PETRASSO, 1988]. Typical values of the diode currents are about a few μA in the central detectors and a few times 10 nA in the edge detectors in ohmic discharges; with auxiliary heating and impurity puffing, the currents come up to a few times 100 μA.

2.2 Pinhole cameras

To get an overview of the radiation from the entire plasma, several pinhole cameras are placed around the poloidal cross-section of the tokamak, as shown in Figure 1 for the ASDEX Upgrade tokamak. Each camera is equipped with a large number of diodes arranged in a semicircle with radius $\Delta = 69.7$ mm around the small pinhole of width $b_1 = 2.0$ mm, length $b_2 = 18.0$ mm, and thickness $b_3 = 0.5$ mm. The characteristic data of the five pinhole cameras with 124 diodes are given in Table 1. The corresponding $p - \phi$ diagram is given in Figure 2.

The different diodes and cameras were calibrated to each other *in situ* with the

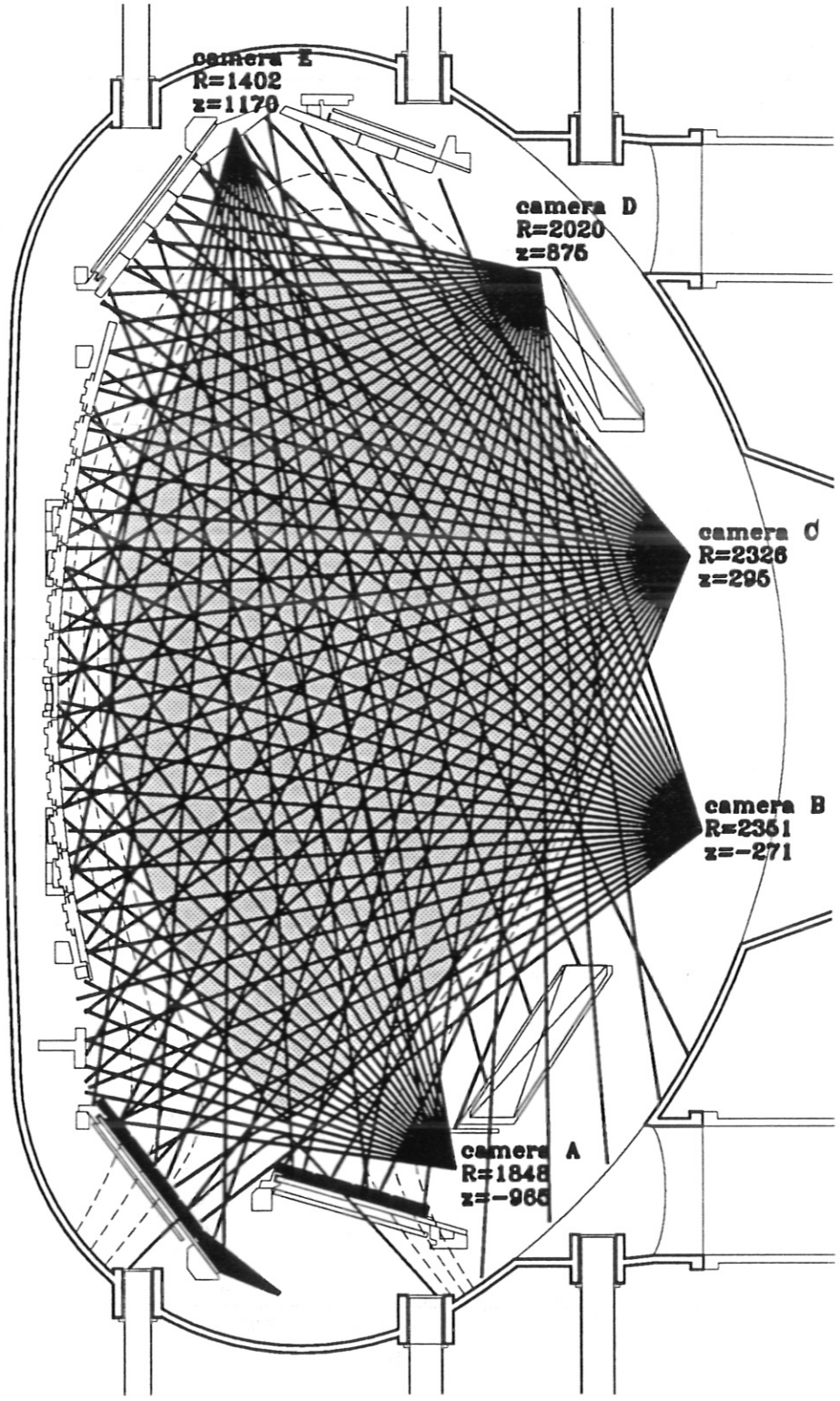

Figure 1: Camera arrangement with 5 cameras and a total of 124 chords around the poloidal cross-section of the ASDEX Upgrade tokamak.

Camera	A	B	C	D	E
Pinhole position					
radius r_0 [m]	1.848	2.351	2.326	2.020	1.402
height z_0 [m]	-0.965	-0.271	0.295	0.875	1.170
Number of diodes	20	30	32	30	12
Angles of chord					
minimum [°]	99.9	107.9	130.1	167.9	254.1
maximum [°]	172.1	218.1	247.9	278.1	295.9
span [°]	72.2	110.2	117.8	110.2	41.8

Table 1: Data of the ASDEX Upgrade pinhole camera system.

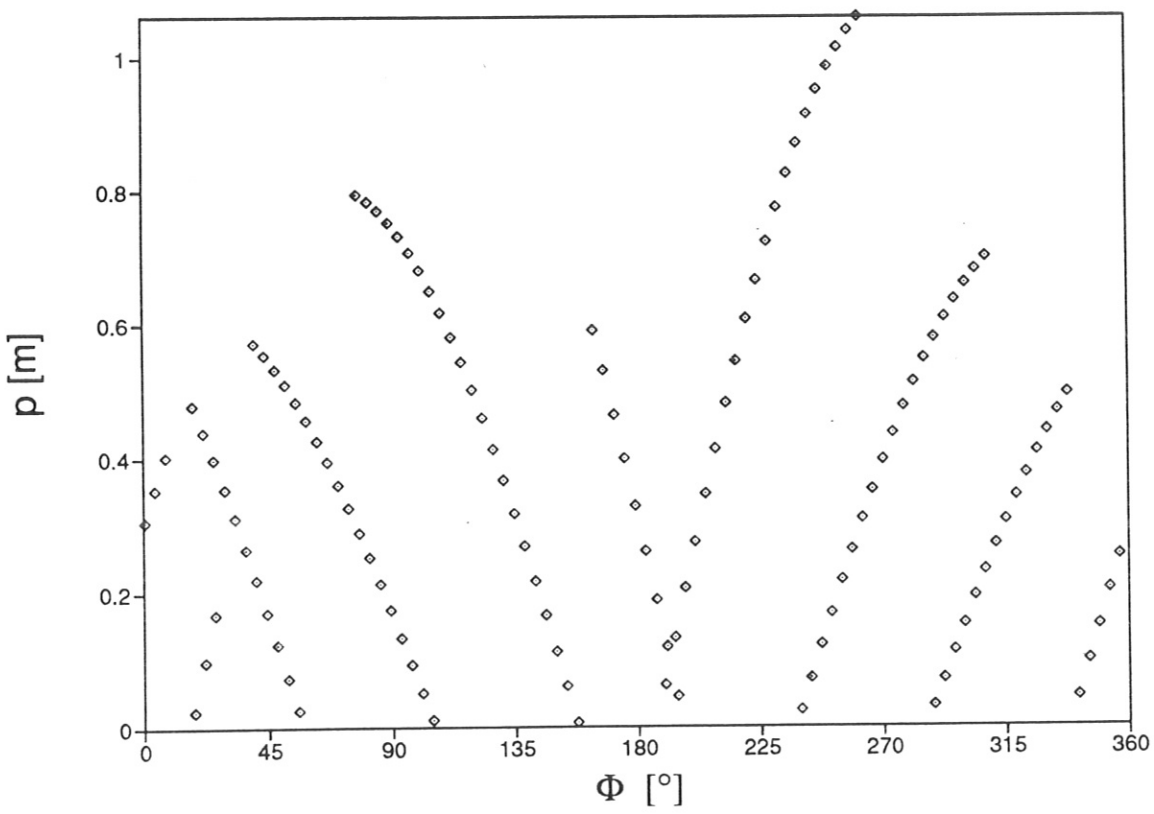

Figure 2: $p - \phi$ diagram showing the arrangement of the 124 diodes in the ASDEX Upgrade tokamak.

help of circular plasmas in different vertical positions.

2.3 Sensitivity

The spectral efficiency of the cameras has an *upper* limit at high energies determined by the thickness of the silicon diode, since high-energetic photons lose only a small fraction of their energy in the diode. A response of 90 % is attained at 10 keV and 50 % at 15 keV. The *lower* limit, however, can be influenced more flexibly. Firstly, it is given by the thickness and the material of the coating on the silicon diode. Secondly, additional foils in front of the pinhole camera can shift the lower limit to higher energies in order to exclude different impurity edges. Without any foils, the pinhole camera system detects radiation over the whole energy range, even visible light from the tokamak edge plasma, since the aluminum coating does not cover the whole surface of the diode. Phenomena such as ELMs or MARFEs are therefore also investigated by this camera system (see Section 6.1). With thin beryllium foils 6 μm thick, the lower limit is shifted to 1 keV for 50 % response and to 3 keV for 90 % response, respectively (see figure 3(a)). Other beryllium foils 100 μm thick shift the lower response edge to 2.5 keV and 5 keV, respectively (see figure 3(b)).

As the detectors integrate the emissivity ϵ of the plasma along their corresponding chord, the observed power density $p_D^{(i)}$ of the i-th diode is a convolution of ϵ with the spectral sensitivities of the camera without (f_{camera}) and with (f_{foil}) applied foils, respectively, namely

$$\begin{aligned} p_D^{(i)}(p,\phi) &= \int dl(p,\phi)\, \epsilon_{sxr}(r,\theta) \\ &= \int dl(p,\phi) \int d(h\nu)\, \epsilon(h\nu; r,\theta)\, f_{\text{camera}}(h\nu)\, f_{\text{foil}}(h\nu). \end{aligned}$$

The i-th detector absorbs a fraction

$$P_D^{(i)}(p,\phi) = p_D^{(i)}(p,\phi)\; A_D\; d\Omega^{(i)}$$

proportional to its area $A_D = d_1 d_2$ and solid angle $d\Omega^{(i)} = A_P^{(i)}/4\pi\Delta^2$. There, the effective pinhole area $A_P^{(i)}$ entering depends on the individual angle α_i along which the i-th diode observes the emissivity. Geometric considerations give

$$A_P^{(i)} = A_P \left(\cos\alpha_i - \frac{b_3}{b_1} |\sin\alpha_i| \right),$$

with $A_P = b_1 b_2$ being the geometric area of the pinhole. Finally, the absolute sensitivity $\gamma_D = 1\text{A}/3.62\text{W}$ determines the current $I_D^{(i)}$ in the i-th diode as

$$I_D^{(i)} = P_D^{(i)} \gamma_D.$$

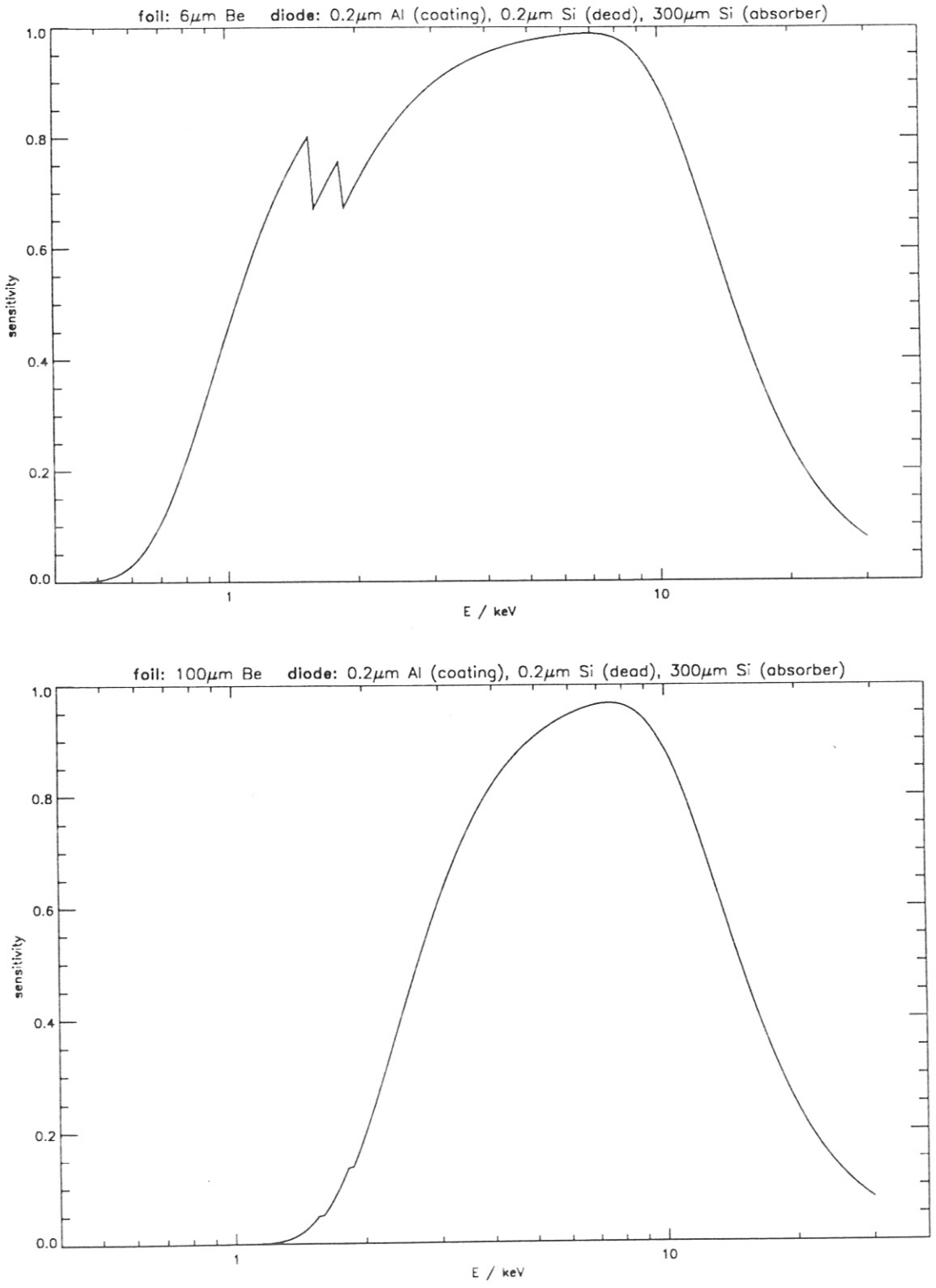

Figure 3: Spectral sensitivity of the diodes from ASDEX Upgrade with (a) 6 μm beryllium foil and (b) 100 μm beryllium foil.

Vice versa, the unknown power density $p_D^{(i)}(p, \phi)$ is calculated as

$$p_D^{(i)} = \frac{P_D^{(i)}}{A_D d\Omega^{(i)}} = \frac{I_D^{(i)}\, 4\pi\Delta^2}{\gamma_D A_D A_P \left(\cos\alpha_i - \frac{b_3}{b_1}|\sin\alpha_i|\right)} \quad . \tag{1}$$

3 Data acquisition

The high temporal resolution with a sampling frequency of 500 kHz, i.e. temporal resolution 2 μs, is a great advantage of the ASDEX Upgrade pinhole diagnostics. The former ASDEX pinhole cameras normally operated with a sampling frequency of 200 kHz [BÜCHSE, 1991].

3.1 Electronics

The current I_D of each diode is amplified in two stages. Firstly, a pre-amplifier with a fixed amplification of $\overline{V}_{pre} = 25$ and four selectable resistors with $R_{pre} = 39\Omega$, 620 Ω, 10 kΩ, 160 kΩ transforms the current into an amplified voltage

$$U_{pre} = I_D R_{pre} \overline{V}_{pre}.$$

This voltage is further amplified by the main amplifier with a fixed amplification of $\overline{V}_{main} = 4$ and additional selectable factors $V_{main} = 2^N$ with $N = 0, \ldots, 8$, i.e.

$$U_{main} = U_{pre} \overline{V}_{main} V_{main} + U_0,$$

where an offset $U_0 = 0.1$ V is added. This voltage is transformed by a 12 bit/+10 V analog-to-digital converter into the digital signal

$$S_{sxr} = \gamma_{adc}\, U_{main}$$

with $\gamma_{adc} = 409.5$ bits/V. Putting all the pieces together, we get the relation between the diode current I_D and the digital signal S_{sxr}:

$$I_D = \frac{U_{pre}}{R_{pre}\overline{V}_{pre}} = \frac{U_{main} - U_0}{\overline{V}_{main} V_{main} R_{pre} \overline{V}_{pre}} = \frac{(S_{sxr}/\gamma_{adc}) - U_0}{\overline{V}_{main} V_{main} R_{pre} \overline{V}_{pre}}.$$

The resolution and sensitivity of $S_{sxr,min} = 1$ bit with maximum amplification $R_{pre} =$ 160 kΩ and $V_{main} = 2^8 = 256$ would correspond to a minimum current $I_{D,min} = 6 \times 10^{-13}$ A. The maximum signal $S_{sxr,max} = 4095$ bit with minimum amplification $R_{pre} = 39\Omega$ and $V_{main} = 1$ would correspond to a maximum detectable current $I_{D,max} = 2.5$ mA. The dynamic range is hence about 10 decades!

3.2 Transputer hardware

The acquisition of digital data is performed with a parallel computer based on IMS T800 transputers. Each transputer has a 32-bit cpu with 10 to 20 MIPS integer performance and a 64-bit floating point unit with up to 2.25 Mflop/s; its

9 independent DMA channels, viz. 4 LinkIn, 4 LinkOut and the memory interface, guarantee high performance.

An overview over the parallel transputer computer for the five SXR cameras is depicted in Figure 4. The digital signals of the different diodes enter the parallel

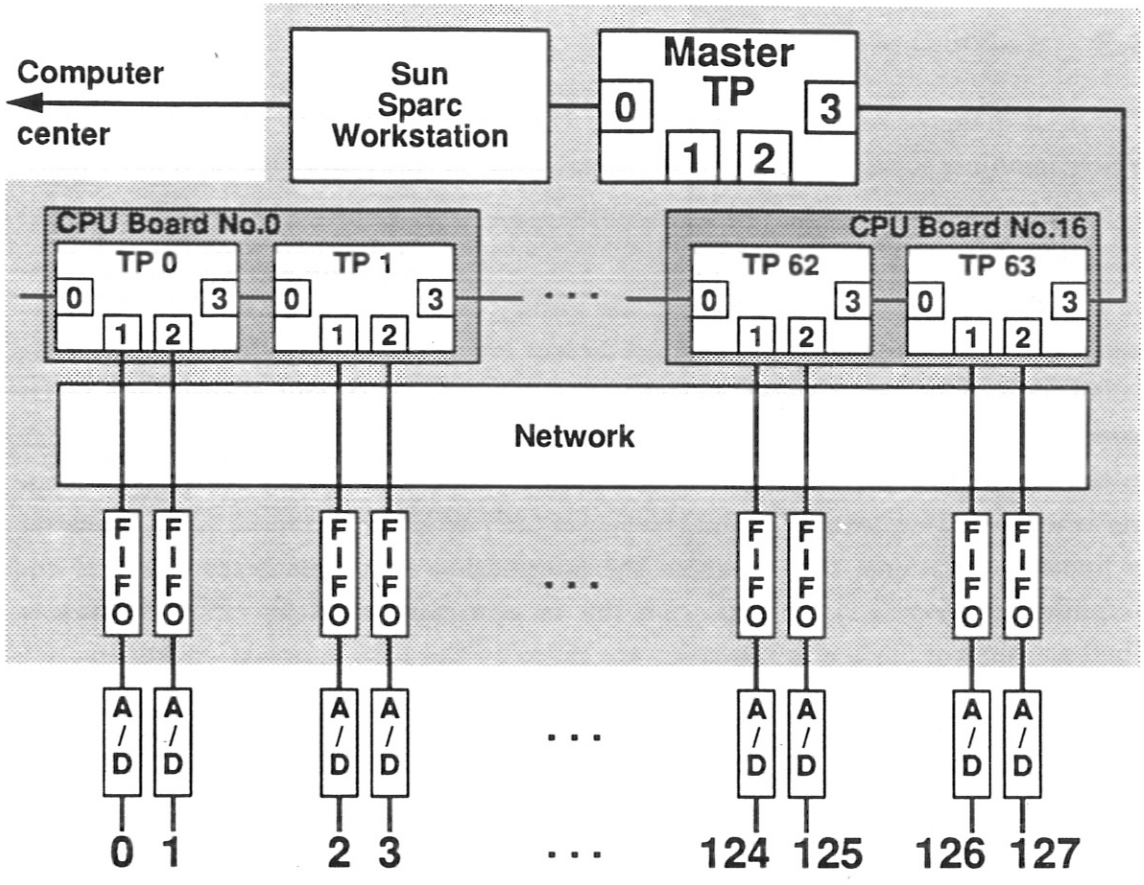

Figure 4: Parallel computer on transputer basis for up to 128 input signals.

computer at fifo modules with 4 kByte RAM; these modules are able to buffer a limited number of data in order to allow the analog-to-digital converter to send data with a continuous high frequency of 500 kHz. After the data pass the configuration network[2], they arrive in the main 16 CPU1 boards. Each CPU1 processor unit contains four transputers and an additional 4 MByte RAM; each of these four transputers registers two data lines. Two of the 128 transputers serve as compensation. The whole transputer system is controlled by the master cpu, which is equipped with one transputer and 4 MByte RAM. A link interface connects this master board with the workstation where the diagnostics is started and controlled.

[2]The configuration network was built in order to change the network at runtime and thereby accelerate the data acquisition. Tests, however, have shown that such a reconfiguration decelerates the data acquisition procedure!

The parallel computer system was designed and is being operated in a co-operation between physicists and computer scientists at IPP. Special thanks to C. Brosig and M. Zilker! The programming of the transputer is performed in OC-CAM [SCHÜTTE, 1988] and is documented in part [NEUPERT, 1991].

3.3 Software environment

The SXR diagnostics is embedded in the ASDEX Upgrade data acquisition system, which combines local SUN workstations and a fast network to IPP Computer Centre.

The SXR workstation in use is a SUN sparc station 10 with a single processor, 64 MByte RAM and 50 MHz frequency. The code for the data acquisition is written in C and relies on the ASDEX Upgrade library calls for shotfile headers. The raw signals together with their calibration factors are written into a level-0 diagnostics called SXR. They are ordered as signal groups A, B, C, D, and E according to the corresponding camera name; the indices from 1 to 32 of the signal groups point to the individual diode signal. The individual calibration factors serve to calculate the transformation from S_{sxr} [bit] to p_D [W/m^2] as given by equ. 1. In a hierarchy of linear calibrations, they combine the information about geometry (see 2.3) and amplification (see 3.1) settings with the *in situ* calibration by circular plasmas. Further items of on-line information are given by the ISIS information system.

4 Tomographic reconstruction

In order to determine the local emissivity $\epsilon(R, z; t)$ of the SXR radiation in the plasma, we have to deconvolute the measured signals which are integrals along the lines of sight.

4.1 Bolometric-type deconvolution

As a first attempt, two-dimensional deconvolution is performed with the same tomographic algorithm as applied to the radiation profiles of the bolometers [FUCHS *et al.*, 1994]. This algorithm relies on the fact that the emissivity varies much less along field lines than perpendicular to them. This behavior may be described by an anisotropic diffusion model with strongly different values of the diffusion coefficient along ($D_{||}$) and perpendicular ($D_{\perp}$) to the magnetic field lines. Sources and sinks (s) are minimized by considering the measured line integrals. The model is thus limited to neither symmetric radiation profiles nor closed magnetic surfaces. It calculates the local emissivity ϵ for different time slices t as snapshots.

The diffusion equation

$$\nabla \cdot \mathbf{F} := \nabla \cdot (D \nabla \epsilon) = -s + \frac{\partial \epsilon}{\partial t}$$

is split into parallel and perpendicular contributions (with respect to flux surfaces), i.e.

$$\mathbf{F} = \mathbf{n}\, D_{\perp}\ (\mathbf{n} \cdot \nabla \epsilon) + \mathbf{t}\, D_{||}\ (\mathbf{t} \cdot \nabla \epsilon)$$

with $\mathbf{n}$ and $\mathbf{t}$ being the normal and tangential vectors to the flux surface, respectively.

The model minimizes the expression

$$Q \;=\; \int dR\, dz\, (\nabla \cdot \mathbf{F})^2 + A \sum_{i=1}^{N} \left(\frac{p_{calc}^{(i)} - p_{meas}^{(i)}}{\delta^{(i)}\, p_{meas}^{(i)}} \right)^2 \;=:\; I + A\, S,$$

with $p_{calc}^{(i)} = \int dl^{(i)}\, \epsilon$ being the calculated line integral, and $\delta^{(i)}$ the assumed relative error. The weight factor A between the flux integral I and the difference S between measurement and calculation is determined iteratively from, for example,

$$\sum_{i=1}^{N} \left(\frac{p_{calc}^{(i)} - p_{meas}^{(i)}}{\delta^{(i)}\, p_{meas}^{(i)}} \right)^2 \approx N.$$

Performing the minimization task on a rectangular grid (R_i, z_j) reduces it to the solution of a system of linear equations.

This tomographic algorithm is implemented in Fortran for a 25×47 grid; it needs about 30 MByte memory space and roughly 10 min cpu time on a SUN sparc ELC workstation or 10 s on a CRAY Y-MP. SXR emissivity profiles $\epsilon(R, z)$ as well as the total radiated power in the core plasma are stored in a level-1 diagnostics SXZ built up in the same way as the corresponding emissivity profile BSZ measured by bolometers.

4.2 Rotational tomography in natural coordinates

The bolometric deconvolution, however, yields the reconstructed emissivity on a *snapshot* basis, i.e. the high temporal dynamics cannot be followed so easily, and needs some model assumptions. Other reconstruction algorithms are therefore under discussion. Two different approaches are considered.

In order to avoid assumptions on the spatial structure of the emissivity profile, *algebraic* iterative schemes are used. The *maximum entropy* method is probably the most developed technique in this category [KAPUR, 1989, LINDEN *et al.*, 1994]. The algebraic methods have two main drawbacks: high computer time consumption and the possibility of non-real solutions. To overcome these drawbacks, the equilibrium flux distribution is used as a first guess for the emissivity profile, which allows a saving of computer time and guarantees in a sense that a realistic solution is obtained; this has been quite successfully applied to the W7-AS stellarator [NAVARRO *et al.*, 1991].

Modal techniques usually use firstly the assumption that the SXR emissivity is constant on flux surfaces and secondly apply an expansion of the emissivity in Zernicke polynomials [GOOT *et al.*, 1989, KUO-PETRAVIC, 1988]. With respect to the second point, the Cormack inversion with Zernicke polynomials suffers from the fact that large spurious images may appear near the boundary and many expansion terms are required. Therefore, Bessel functions are proposed as base functions [NAGAYAMA, 1987] with the advantage that the inversion is less sensitive to the noise at the boundary and fewer terms save computing time. Concerning the first point, the underlying assumption is only justified for the core plasma, where the safety factor q is low.

In order to improve the spatial resolution of the modal reconstruction, rotational tomography has been proposed [SMEULDERS, 1983]. This is based on the assumption that the plasma rotates rigidly in the toroidal or poloidal direction. This brings up additional *virtual* chords for the reconstruction. In the case of concentric circular flux surfaces, the formalism is straightforward and analytical. It is valid for the whole plasma volume and has been applied to many tokamaks

[KRAUSE *et al.*, 1988, NAGAYAMA *et al.*, 1990, BÜCHSE, 1991]. The analytical solution, however, can only persist if the deviations from the assumed topology of concentric circular flux surfaces remain small. This restricts its validity to a small Shafranov shift, constant elongation κ, and zero triangularity δ, i.e. the plasma core. Outside this core, the rigid toroidal rotation does not lead to a rigid rotation in the reconstruction plane, and therefore no analytical solution can be given.

We generalize the idea of rotational tomography to arbitrary plasma shape by using the "natural" magnetic coordinates [D'HAESELEER *et al.*, 1991]: The radial coordinate must be a label of the magnetic flux, e.g. ρ_{pol}, and the poloidal coordinate is the *straight field line angle* θ^* defined by the condition $d\theta^*/d\phi = \text{const}$ along a magnetic field line, with ϕ being the ignorable toroidal coordinate. In the coordinates (ρ_{pol}, θ^*) the chords become curved, as can be seen in Figure 5.

For the reconstruction algorithm, the emissivity is expanded in harmonics in the θ^*-direction. In the radial direction, an ansatz of an arbitrary cubic spline with fixed nodes is utilized. The code development is now in its final phase. More details on and results from this generalized reconstruction will be given in the Ph.D. thesis of M. Sokoll.

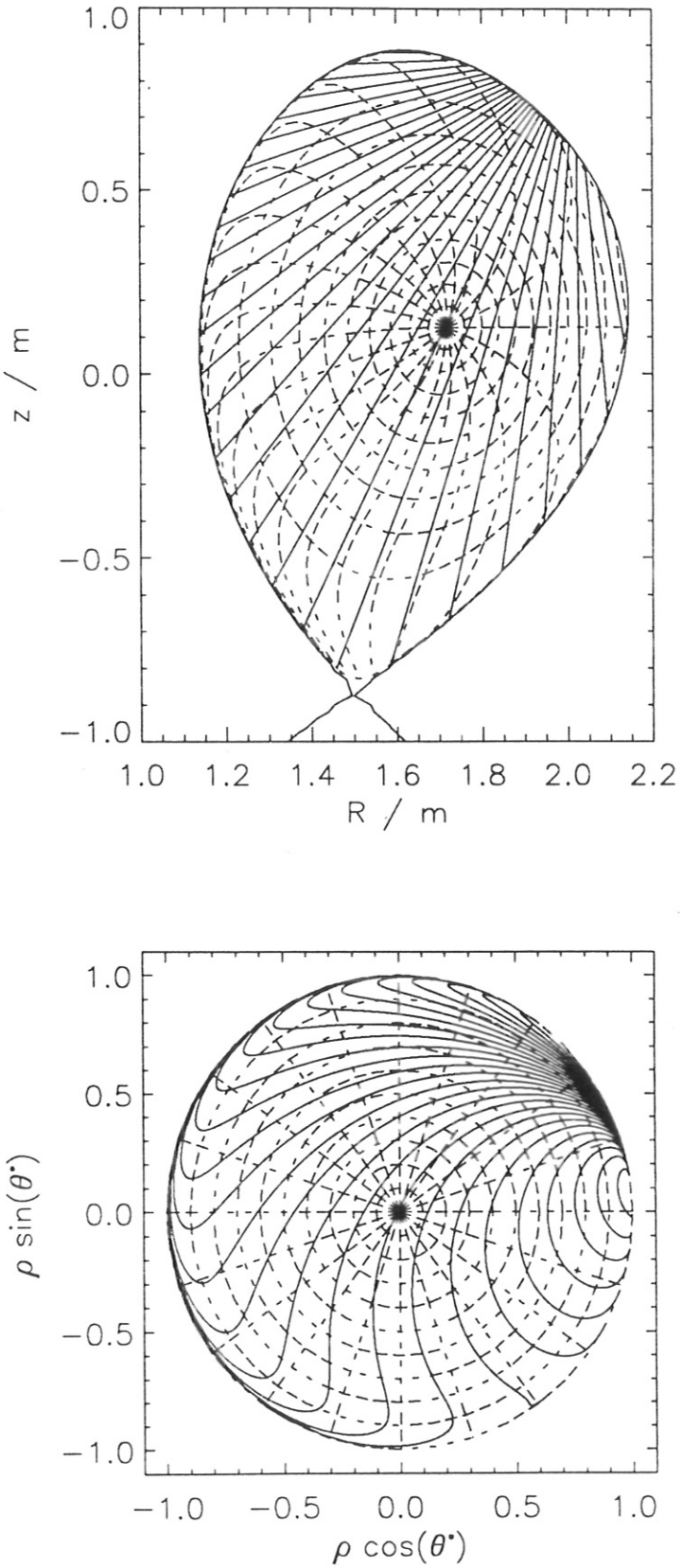

Figure 5: Geometry of the chords of the SXR camera D (a) in real (R, z)-plane and (b) in a poloidal plot of (ρ, θ^*) coordinates.

5 Further data analysis

As usual, further data analysis is done by FFT. More complex analysis are based on wavelet transformations; results will be given in the Ph.D. thesis of K. Hallatschek.

In addition, singular value decomposition has been performed in order to determine temporal as well as spatial eigenvectors of MHD structures. Results for sawtooth activity are given in [BESSENRODT-WEBERPALS *et al.*, 1994] and for ($m = 1, n = 1$) MHD-mode analysis in [BESSENRODT-WEBERPALS *et al.*, 1995].

6 First results

First results of the SXR camera system described above will now be discussed firstly with respect to the fast time response and secondly with respect to emissivity profiles.

6.1 Fast dynamics

As an example of the investigations of fast events, the observations of ELMs in a quasi-stationary H-mode discharge (#4789: $I_p = 1.0$ MA, $B_t = 2.0$ T, $P_{\text{aux}} \leq 10$ MW) with strong type-I ELM activity are shown in Figure 6. The events are seen on

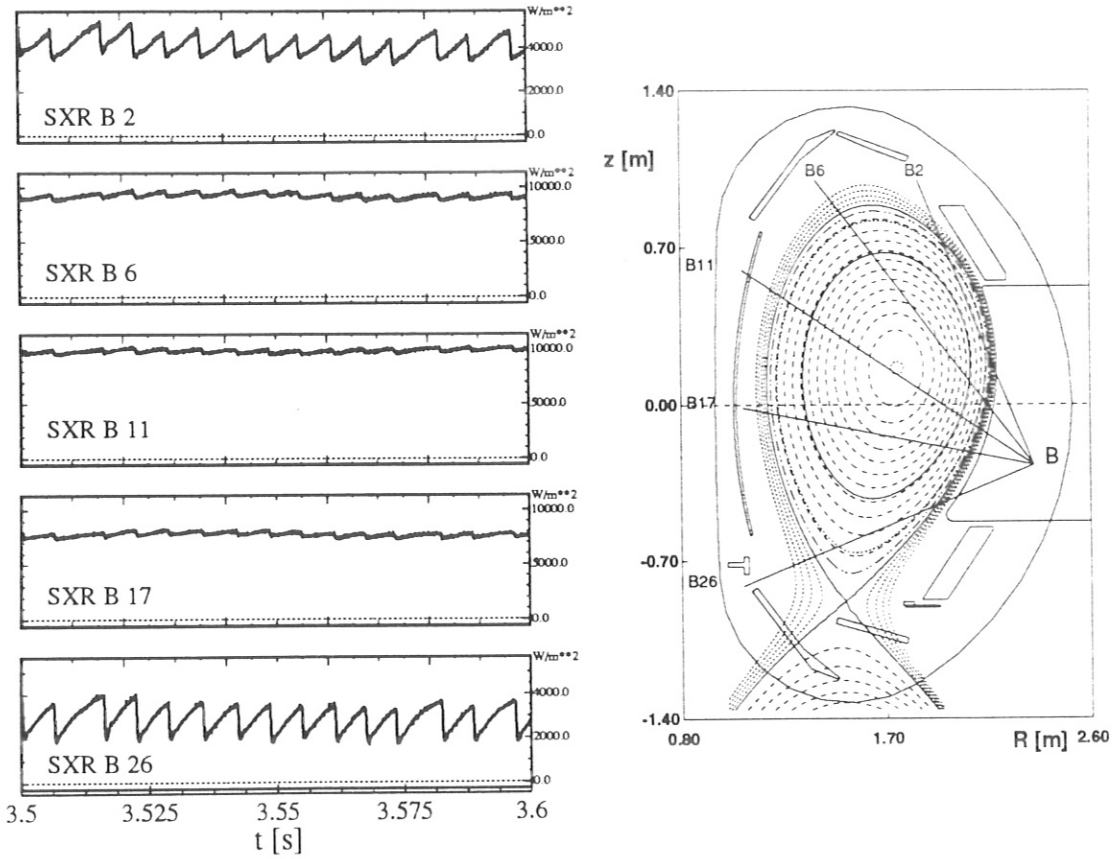

Figure 6: Observations of ELMs in a quasistationary H-mode discharge (#4789: $I_p = 1.0$ MA, $B_t = 2.0$ T, $P_{\text{aux}} \leq 10$ MW) with strong type-I ELM activity.

nearly all chords of the different cameras. The modulation is stronger and reaches about 50 % for the outer chords as compared with the few % modulation for the central chords. The period is determined to be about 6 ms for these type-I ELMs, which agrees well with the H_α measurements in the divertor.

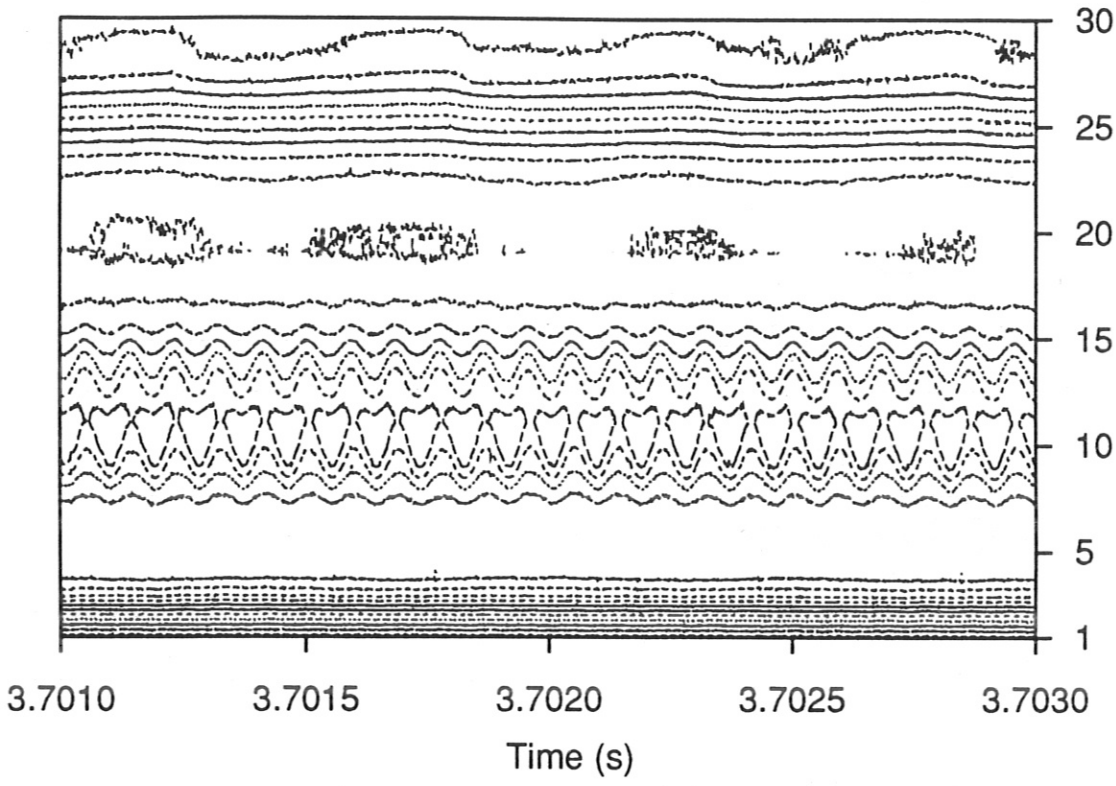

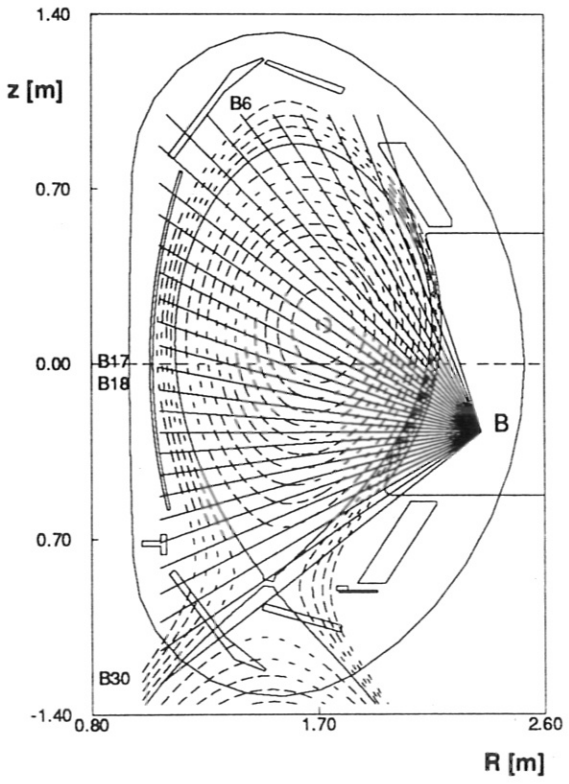

Figure 7: Observations of weak and frequent type-III ELMs together with $(1,1)$ MHD-mode activity during the feedback-controlled neon puffing into an H-mode discharge (#4881: $I_p = 1.0$ MA, $B_t = 2.5$ T, $\overline{n}_e = 11.8 \times 10^{19}$ m^{-3}, $P_{\mathrm{aux}} \leq 8$ MW).

During feedback-controlled neon puffing, the ELMs change to weak and frequent type-III ELMs which have a reduced period of about 0.5 ms, i.e. 2 kHz. As a paradigm, Figure 7 shows a contour plot of the SXR radiation detected by camera B during 2 ms in the feedback-controlled neon puffing phase of an H-mode discharge. Four ELMs are observed in the boundary (chords B18 to B30) together with about 23 periods of the rotating helical (1,1) MHD-mode (chords B6 to B17). For clarity, the camera geometry is also depicted. These type-III ELMs cannot be seen any more in the H_α light in front of the divertor plates if the plasma is completely detached. Compared with the type-I ELMs, it looks as if the weaker type-III ELMs have their inversion radius at one SXR chord further outside than the stronger type-I ELMs.

6.2 Radiation profiles

We applied the bolometric-type tomographic reconstruction (see Section 4.1) to calculate paradigmatically the SXR emissivity profiles (W/m^3) during the feedback-controlled neon puffing into an H-mode discharge (#4881: $I_p = 1.0$ MA, $B_t = 2.5$ T, $\overline{n}_e = 11.8 \times 10^{19}$ m^{-3}, $P_{aux} \leq 8$ MW), as shown in Figure 8. The contour plots show at the beginning ($t = 2.7$ s) the build-up of a radiation belt according to the neon radiation. In later phases of the same discharge ($t = 3.1$ s, 3.4 s, 3.7 s), a central peak appears which is correlated to a rotating helical ($m = 1, n = 1$) mode and strong density peaking. This central maximum saturates at about 3.7 s and remains after the switch-off of the neon puffing ($t = 4.1$ s).

This evolution is also depicted in Figure 9 in a three-dimensional profile of the emissivity, which compares the situations before ($t = 2.05$ s), during ($t = 3.1$ s and $t = 3.7$), and after ($t = 4.55$ s) the feedback-controlled neon puffing. These observations point to the fact that the CDH-mode in ASDEX Upgrade successfully combines the well-known H-mode transport barrier at the edge with an impurity-forced improvement in the core confinement; the latter has also been found in L-mode discharges.

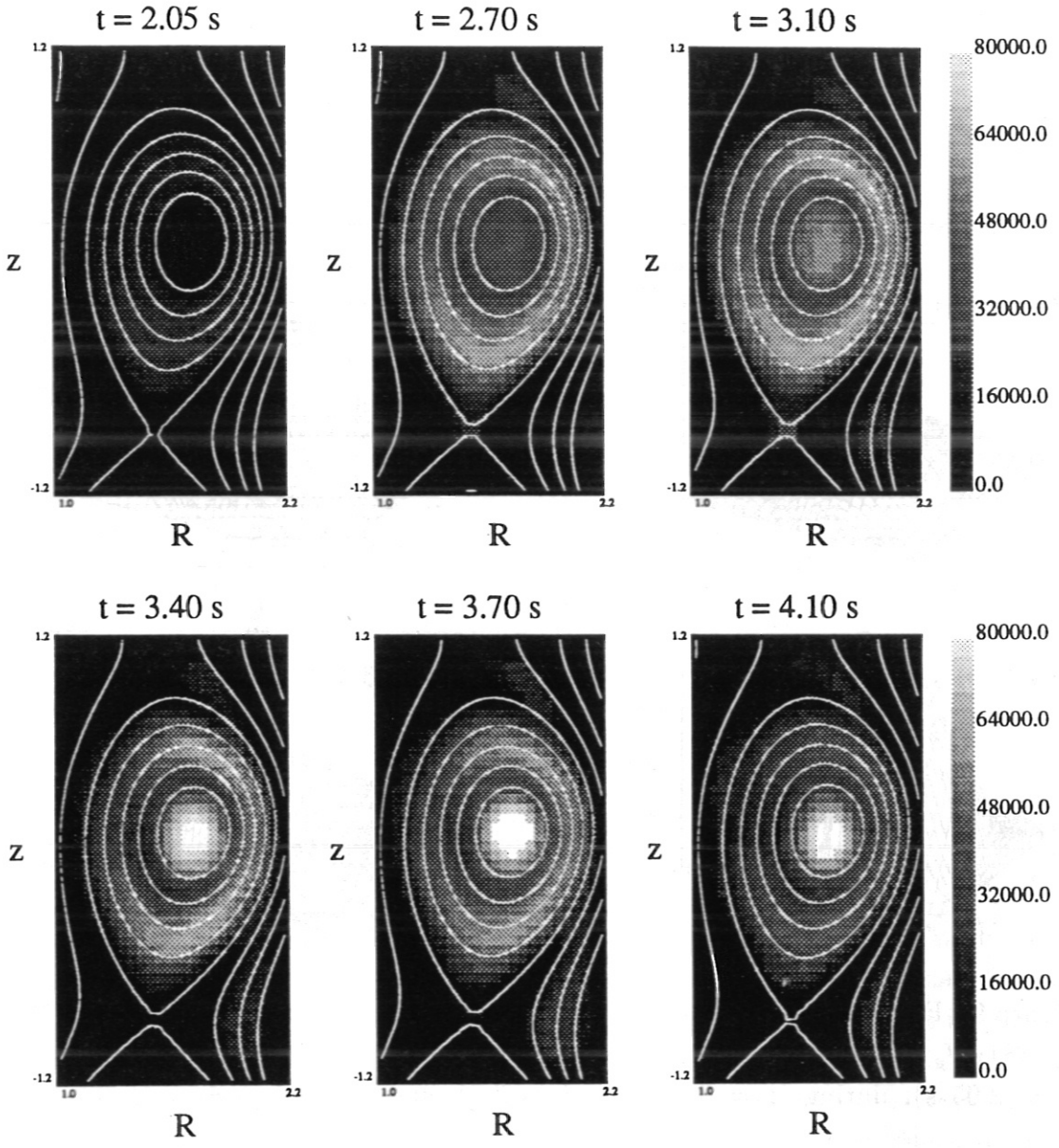

Figure 8: Evolution of the soft X-ray emissivity (W/m^3) before (t = 2.05 s), during (t = 2.7 s, 3.1 s, 3.4 s, 3.7 s) and after (t = 4.1 s), the feedback-controlled neon puffing into an H-mode discharge (#4881: I_p = 1.0 MA, B_t = 2.5 T, $\overline{n}_e = 11.8 \times 10^{19}$ m^{-3}, $P_{\text{aux}} \leq 8$ MW).

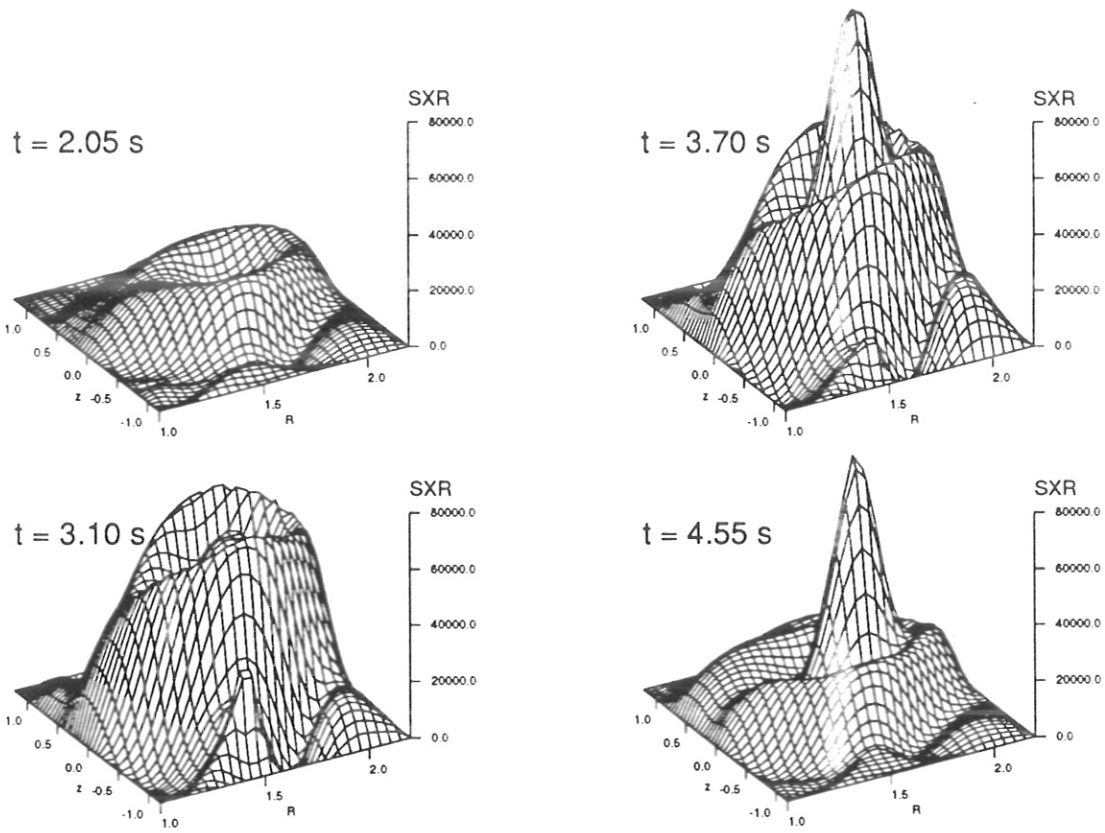

Figure 9: Evolution of the soft X-ray emissivity (W/m^3) in an H-mode discharge (#4881: $I_p = 1.0$ MA, $B_t = 2.5$ T, $\overline{n}_e = 11.8 \times 10^{19}$ m^{-3}, $P_{\mathbf{aux}} \leq 8$ MW) before ($t = 2.05$ s), during ($t = 3.1$ s and $t = 3.7$), and after ($t = 4.55$ s) the feedback-controlled neon puffing.

7 Summary and Conclusions

This report describes the set-up of the soft X-ray pinhole camera system for the ASDEX Upgrade tokamak with respect to detectors, cameras, electronics, and data acquisition by parallel computers. The SXR diagnostics provides good temporal as well as spatial resolution for the emissivity from the hot plasma.

As a paradigm, first results of the recent CDH-mode discharges in ASDEX Upgrade with feedback-controlled neon puffing have been presented. They are characterized by frequent and weak type-III ELMs in the outer plasma zones and a rotating helical (1,1) MHD structure in the core plasma.

Acknowledgements

We are indebted to M. Kornherr and H. Krause for their contributions to the preliminary set-up of the SXR system. We would like to thank J. Krippner for his devoted work to mechanical constructions, E. Buchelt and G. Schramm for developing the electronics, and K. Behler, H. Blank, and R. Merkel for providing us with the necessary workstation and software facilities. With respect to the transputer-based parallel computer, we would like to thank our colleagues from the Computer Science Division, namely C. Brosig, and M. Zilker, for their continuous support with hardware and software tasks.

The authors gratefully acknowledge the discussions with T. Cho (University of Tsukuba, Japan), Christian Fuchs, H.-J. Fahrbach, J. Gernhardt, M. Maraschek, M. Schittenhelm, S. Sesnic (Princeton), A. Weller, H. Zohm.

It is a pleasure to acknowledge the excellent support from the whole ASDEX Upgrade Team.

References

[Bessenrodt-Weberpals *et al.*, 1995] Bessenrodt-Weberpals, M., de Blank, H. J., McCarthy, P., Sokoll, M., and the ASDEX Upgrade Team, Analysis of rotating ($m = 1, n = 1$) modes as seen in soft X-ray radiation and its application to current profile identification, *Europhys. Conf. Abstr.* .

[Bessenrodt-Weberpals *et al.*, 1994] Bessenrodt-Weberpals, M., Maraschek, M., Zohm, H., the ASDEX Upgrade Team, and the NI Team, Sawtooth filtering by singular value decomposition, *Europhys. Conf. Abstr.* **18B, Pt. III**, 1312–1315.

[Büchse, 1991] Büchse, R. (1991). *Tomographische Untersuchungen interner Disruptionen an den Tokamaks ASDEX und TFTR.* PhD thesis, Techn. Universität München. Report IPP-Garching III/175.

[D'haeseleer *et al.*, 1991] D'haeseleer, W. D., Hitchon, W. N. G., Callen, J. D., and Shohet, J. L. (1991). *Flux coordinates and magnetic field structure.* Springer, Berlin.

[Fuchs *et al.*, 1994] Fuchs, J. C., Mast, K. F., Hermann, A., and Lackner, K., Two-dimensional reconstruction of the radiation power density in ASDEX Upgrade, *Europhys. Conf. Abstr.* **18B, Pt. III**, 1308–1311.

[Goot *et al.*, 1989] Goot, E. v. d., Edwards, A. W., and Holm, J. (1989). Real time application of transputers for soft x-ray tomography in nuclear fusion research. Technical Report P(89)45, JET.

[Kapur, 1989] Kapur, J. N. (1989). *Maximum-entropy models in science and engineering.* Wiley, New York.

[Krause *et al.*, 1988] Krause, H., Kornherr, M., Team, A., and Team, N., High-resolution sparse channel tomography for slowly varying rotating SXR profiles, *Europhys. Conf. Abstr.* **12B, Pt. III**, 1179–1182.

[Kuo-Petravic, 1988] Kuo-Petravic, G. (1988). Soft x-ray tomography on TFTR. Technical Report 2555, PPPL, Princeton.

[Linden *et al.*, 1994] Linden, W. v. d., Ertl, K., and Dose, V. (1994). Maximum entropy reconstruction of local emissivity profiles from soft X-ray chord-measurements. In Spatschek, K. H. and Uhlenbusch, J., editors, *Contri-*

butions to High-Temperature Plasma Physics, pages 131–142, Berlin. Akademie Verlag.

[NAGAYAMA, 1987] NAGAYAMA, Y., Tomography of $m = 1$ mode structure in tokamak plasma using least-squares-fitting method and Fourier-Bessel expansions, *J. Appl. Phys.* **62**, 2702–2706.

[NAGAYAMA *et al.*, 1990] NAGAYAMA, Y., BÜCHSE, R., CAVALLO, A., FREDRICKSON, E. D., JANOS, A., *et al.*, Image reconstructions of ECE and x-ray signals for high-β plasmas, *Rev. Sci. Instrum.* **61**, 3265–3267.

[NAVARRO *et al.*, 1991] NAVARRO, A. P., OCHANDO, M. A., and WELLER, A., Equilibrium-based iterative tomography technique for soft X-ray in stellarators, *IEEE Transact. Plasma Sci.* **19**, 569–579.

[NEUPERT, 1991] NEUPERT, U. (1991). Steuerungssoftware für die Datenerfassung mit einem Transputer-Multiprozessor.

[SCHÜTTE, 1988] SCHÜTTE, A. (1988). *OCCAM2 Handbuch.* Teubner, Stuttgart.

[SMEULDERS, 1983] SMEULDERS, P. (1983). A fast plasma tomography routine with second-order accuracy and compensation for spatial resolution. Technical Report 2/252, IPP, Garching.

[WENZEL and PETRASSO, 1988] WENZEL, K. W. and PETRASSO, R. D., X-ray response of silicon surface-barrier diodes at 8 and 17.5 keV: Evidence that the x-ray sensitive depth is not generally the depletion depth, *Rev. Sci. Instrum.* **59**, 1380–1387.